Modeling the multiple reflections of radiation between terrains and analyzing the reflection characteristics of a lunar area with low topographic undulation

Yunfei Liu, Qiang Guo and Guifu Wang

Abstract—The stable luminosity of the lunar surface makes the Moon an ideal external calibration source. Nevertheless, the albedos of the mare and the highlands are very different. A modeling method based on the lunar global irradiance/reflected radiance is bound to result in higher uncertainty. In contrast, if the local calibration of the lunar surface is adopted, the lunar complex topography effect cannot be ignored. Based on the adjacent terrain irradiance formula of the first-order reflection proposed by Proy, the second-order to the *nth*-order reflections of radiation between terrains are derived in this paper, and incident radiation received by the terrain surface is quantified. It is concluded that the observation reflectance of low-spatial-resolution remote sensing pixels is a function of the real reflectance of the microtopography within the pixel, terrain roughness, solar incidence angle, and remote sensing observation angle. Simulation experiments show that for the same illumination observation geometry, the radiance after multiple reflections is often several percentage points higher than that after the first reflection. This finding demonstrates the importance of considering multiple reflections in retrieving the true reflectance of terrains. In addition, the reflectance curve of the new model is very similar to that based on Chang'e-3 in situ measurements, and the relative error of the results is between -3.7% and -6.3%. This proves the accuracy of the new model. The research results presented in this paper can aid in correcting reflectance in remote sensing pixels and provide important reference significance for the construction of surface BRDF.

Index Terms—Effect of microtopography inside remote sensing observation pixels, multiple-reflection-process modeling of radiation between terrains, and characteristics of reflected radiance in the lunar surface region

I. Introduction

THE Moon is an ideal external calibration source for remote sensing instruments because of its stable surface luminosity and lack of atmospheric influence. Radiometric calibration methods that observe the Moon in reflective solar bands have undergone extensive development. The Robotic Lunar Observatory (ROLO) model is the model with the highest calibration accuracy worldwide, and its uncertainty is 5–10% [1]. Nevertheless, as the required calibration accuracy continues to rise, the limitations of this model's calibration accuracy have been reached [2]. To improve the ROLO model, Zhang et al. [3] proposed using the mean equigonal albedo to replace the reflectance of Apollo soil samples; the new model's irradiance values in the VNIR bands are closer than those of the traditional ROLO model to the observations from the Moderate Resolution Imaging Spectroradiometer (MODIS) and Sea-viewing Wide Field-of-view Sensor (SeaWiFS). Sun et al. [4] developed a new model based on MODIS instrument observations to compensate for the shortcomings of the ROLO model in lunar irradiance measurement, which significantly improved the MODIS lunar calibration results of the entire mission. However, the albedos of mare and highlands are very different, and the relationship between the albedos change and the observation geometry varies. A modeling method based on the global irradiance/reflected radiance of the Moon is bound to result in higher uncertainty. The details of the luminosity properties of the lunar surface are complicated by the macroscopic roughness of the Moon [5]. According to different terrane types of the lunar surface, Wu et al. [6] divided the moon into four classes of albedo type and established a lunar irradiance model based on Chang'e-1 imaging interferometer (IIM) data; however, their model has some shortcomings in that the wavelength range is too narrow, and the model errors in high-latitude areas and border areas are relatively large. If a local area on the lunar surface is used for calibration, it is necessary to consider incorporating topographic data to study the problem of rim modeling and to improve the irradiance simulation accuracy [6].

Large and small impact craters are densely distributed on the lunar surface [7]. At the meter to hectometer scales, there are obvious differences in the median bidirectional slope, root-mean-square (RMS) height, and median absolute slope between mares and highlands [8]. Rugged terrain often alters illumination and viewing geometry and generates a relief shadow, observation masking, and multiple scattering, which result in intense topographic dependence on the total incident reflectance or radiance [9]–[11]. At present, empirical models such as the Lommel-Seeliger model [12] and Sandmeier model [13] are often adopted for the calibration of lunar photometric observations. Alternatively, the Hapke radiative transfer model

This work was supported by National Natural Science Foundation of China under Grant 41875037 and project for FY-4 ground-based visible and infrared lunar observation system of Shanghai Institute of Technical Physics, Chinese Academy of Sciences (No. O9KCE033N3). (Corresponding author: Qiang Guo.)

Manuscript received April 19, 2021; revised August 16, 2021

with simplified parameters or other models can be used [14]. Empirical models are often prone to overcorrection due to their simple parameters [15], [16], but the Hakpe model [17]–[20] is difficult to apply due to its numerous parameters, mathematical coupling, and high requirements regarding observation data [14].

In ground remote sensing detection, Pory et al. [21] assumed that the surface was Lambertian and proposed that the radiation received by a surface consists of direct solar radiation, scattered atmospheric radiation, and adjacent terrain-reflected radiation. The reflected radiation from the surrounding terrain is defined as the sum of the solar radiation reflected on the target pixel by other visible pixels. Nevertheless, the calculation of reflected radiation from the surrounding terrain only considers the first-order scattering effect between terrains. The attenuation of the signal between two adjacent slopes and second-order reflection are neglected [21] (see formula (4)). In remote sensing on Earth, the multiple reflections of radiation between terrains are often attenuated greatly due to the influence of air, but for the lunar surface without atmospheric influence, the multiple reflections of radiation between terrains should be given more attention.

In this paper, a new model for quantifying multiple reflections of radiation between terrains is presented. Based on the adjacent terrain irradiance formula of the first-order reflection proposed by Proy, the second-order to the *nth*-order reflections of radiation between terrains are derived. Moreover, the expression of the quantitative relationships among the incident irradiance of each surface and the number of reflections of radiation between terrains, and the number of mutually visible slopes is established. It is concluded that the observed reflectance in low-spatial-resolution remote sensing pixels is a function of the real reflectance of the microtopography inside each pixel, terrain roughness, solar incidence angle, and remote sensing observation angle. The influencing factors are the initial incident irradiance of the terrain surface under solar illumination, multiple reflection effects caused by terrain undulation, and observation masking. Simulation experiments show that for the same illumination observation geometry, the radiance after multiple reflections is often several percentage points higher than that after the first reflection. This finding demonstrates the importance of considering multiple reflections of radiation between terrains in retrieving the true reflectance of terrains. In addition, the reflectance curve of the new model is very similar to that for Chang'e-3 in situ measurements, and the relative error of the results is between -3.7% and -6.3%. This proves the accuracy of the new model.

The research results in this paper can aid in correcting the reflectance values of remote sensing pixels and provide important reference significance for the construction of a bidirectional reflectance distribution function (BRDF) on the surface.

II. Theory

Direct solar radiation over rugged terrain is the most important component of the total incident radiation that reaches the surface. For flat surfaces, the magnitude of direct solar radiation depends on the relative local incident angle between the sun and the normal of the slope surface [11]. Therefore, direct solar radiation changes with different surfaces and slopes [21]. Moreover, the adjacent terrain-reflected irradiance increases the total radiation reaching the slope surface. As shown in Fig. 1, M and P are line-of-sight visible. If either M or P has a radiant emittance greater than 0, reflectance will occur at the other location (assuming no attenuation along the radiative transmission path on the Moon). This indicates that a definite reflection relation exists between the definite terrains. This is why the terrain configuration factor was derived in previous research [22], [23].

The process of reflecting radiation from terrain to terrain stops when the reflected radiation is zero. Obviously, for the lunar surface, the reflection of solar incident radiation between slopes takes place many times.

Assuming that the total solar incident radiation flux of the target terrain is Φ_{sun} (limited area size and no other incident radiation source), the total radiation flux of the first reflection is Φ_1, and after k reflections, the total radiation flux is Φ_k. The relationship among Φ_{sun}, Φ_1 and Φ_k can be expressed by the following formula:

$$\Phi_{sun} > \Phi_1 > \Phi_2 > \cdots > \Phi_k \tag{1}$$

and

$$\Phi_{sun} > \Phi_1 + \Phi_2 + \cdots + \Phi_k \tag{2}$$

where Φ_k infinitely approaches zero.

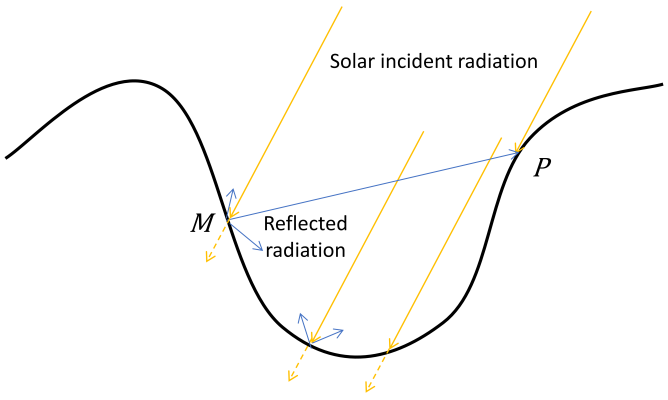

Fig. 1. Slope M reflects radiation to slope P, and M adds a source of irradiation for P. The solid yellow line is the solar incident radiation; the yellow dotted line is the absorbed solar radiation; the solid blue line is the radiation reflected by the terrain.

If we divide the target terrain into equal spatial intervals, multiple microareas with different topographic slopes, topographic aspects, and elevation values can be obtained. The surface-incident radiation on these slopes

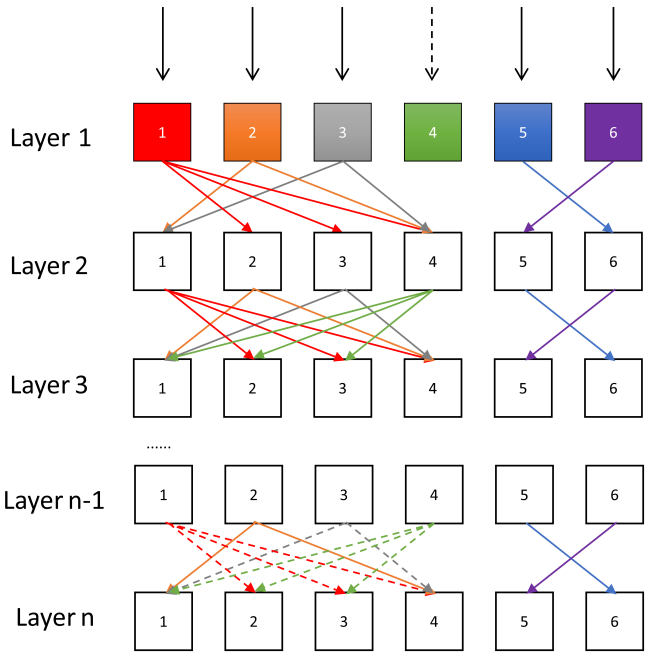

Fig. 2. Schematic representation of an "update" of a radiative source for a microarea. The dashed lines represent that there is no incident radiation, and the solid lines indicate that there is incident radiation. Different colors of the arrows represent the reflected radiation from different microareas, in which the microareas pointed by arrows represent there is a line-of-sight visible. In contrast, the microareas with no arrows represent there is not a line-of-sight visible. The first layer receives the solar incident radiation, and the second to n-th layers receive the reflected radiation from other slopes in the previous layer.

varies with each reflection (see Fig. 2). In this paper, a change in incident radiation on the surface of a microarea is called an "update" of the incident radiation on the surface of the microarea.

A. Updating the incident radiation on the surface of a microarea

1) One-time reflection between terrains: The surfaces are assumed to be Lambertian. As shown in 1, the radiance received by point M and coming from the point P can be written as:

$$L_{(P\to M)} = \frac{L_P \cdot dS_M cosT_M \cdot dS_P cosT_P}{r_{MP}^2} \tag{3}$$

where dS_M and dS_P are the areas of pixels M and P, respectively; T_M and T_P are the angles between the normal to the ground and the line MP; L_P is the luminance of P; and r_{MP} is the distance between M and P. If ρ_P is the reflectance of pixel P illuminated by the irradiance E_P, then $L_P = \rho_P E_P/\pi$. The subscript $P \to M$ represents the transfer of radiation from P to slope M.

Therefore, the total irradiance received by slope M from all "visible" P [21] can be written as:

$$E_M = \sum_j \frac{L_{(P_j\to M)}}{dS_M} = \sum_j \rho_{P_j} \frac{E_{P_j} cosT_M cosT_{P_j} dS_{P_j}}{\pi r_{MP_j}^2} \tag{4}$$

2) Multiple reflections between terrains: As noted in the previous section, if $\rho_M \Phi_M$ is not 0 (where ρ_M is the reflectance of M and Φ_M is the total incident radiation flux received by the slope M from other visible slopes after one-time reflection), then $\rho\Phi_M$ will continue to participate in the next reflection with other slopes. Therefore, the incident irradiance on each microarea surface after each radiation reflection can be obtained, as follows:

$$E_M(1) = E_{(sun\to M)}, \qquad E_{P_j}(1) = E_{(sun\to P_j)} \tag{5a}$$

$$E_M(n) = \sum_j \rho_{P_j} \frac{cosT_M cosT_{P_j} dS_{P_j}}{\pi r_{MP_j}^2} \cdot E_{P_j}(n-1) \tag{5b}$$

where $E_M(n)$ represents the total incident irradiance received by the slope M surface for the n-th time.

Let

$$\Gamma_{MP_j} = \frac{cosT_M cosT_{P_j} dS_{P_j}}{\pi r_{MP_j}^2} \tag{6}$$

where Γ_{MP_j} can be considered the visible radiation factor between P_j and M. Obviously, Γ_{MP_j} does not vary with the number of reflections. Formula (5b) can be simplified as:

$$E_M(n) = \sum_j \rho_{P_j} \Gamma_{MP_j} \cdot E_{P_j}(n-1) \tag{7}$$

Then, after the multireflection between terrains, the total reflected radiance $L_{M_{ref}}$ of slope M to the sky can be expressed as:

$$L_{M_{ref}} = \frac{\rho_M}{\pi}[E_M(1) + E_M(2) + \cdots + E_M(n)] \tag{8}$$

Formula (8) shows that the solar direct incident irradiance on the slope surface, the mutual visibility between slopes and the reflectivity of slopes directly affect the multiple reflection process and results.

B. Direct solar incident irradiance on microtopography surfaces

Changes in altitude affect the distribution of solar radiation, resulting in sunlit and shaded areas that correspond to bright and dark pixels in remote sensing images [24]. In general, on slopes of rugged terrain, the most important variable controlling incident radiation is the local solar illumination angle [23]. If the sun is not hidden by a local horizon, the local illumination angle θ_s on a slope S with azimuth A is given by:

$$cos\theta_s = cos\theta_0 cosS + sin\theta_0 sinScos(\phi_0 - A) \tag{9}$$

where θ_0 is the illumination angle on a horizontal surface and ϕ_0 is the azimuth of illumination.

Shadows refer to regions lacking direct solar illumination, which can be attributed to two reasons: opposing the sun and cast by obstructions [25]. As shown in Fig. 3, for any slope, the received solar irradiation can be divided into

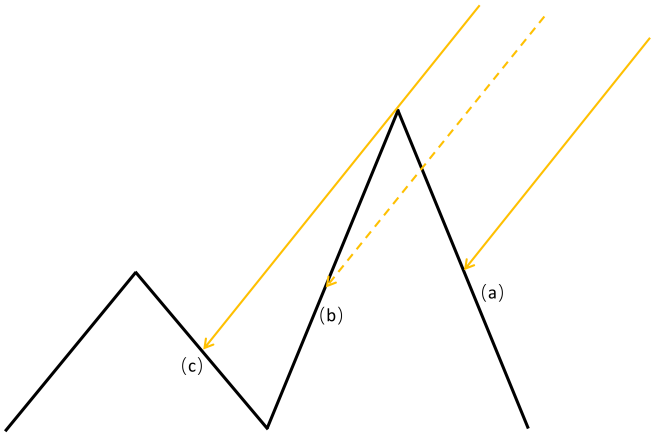

Fig. 3. There are three types of cases in which any slope receives solar radiation: (a) fully irradiated, (b) no irradiation, and (c) partially irradiated.

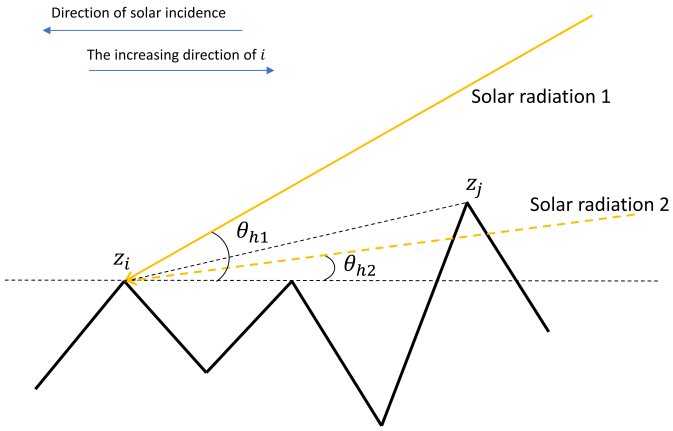

Fig. 4. Schematic diagram of the relationship between the new slope formed and solar radiation. θ_{h1} and θ_{h2} are the altitude angles of solar incident radiation 1 and 2, respectively.

three types: (i) fully irradiated, (ii) partially irradiated, and (iii) no irradiation. First, it is determined whether the two ends of a slope can be irradiated, and the result is used to establish the actual irradiated condition of the slope.

1) Incident irradiance of a one-dimensional terrain surface: We form grid points with elevation values. For a grid row, an elevation function z is defined for the points $j = 0, 1, \ldots, N-1$. Since the points are evenly spaced, the abscissa is specified by $j\Delta h$ [23]. A binary factor Θ is established to indicate whether the elevation point z_j is irradiated. When $\Theta = 1$, z_j is irradiated; when $\Theta = 0$, z_j is not irradiated.

Therefore, for all $0 \leq i < N$, when the direction of solar incidence is the opposite of the increasing direction of i:

(i) for all $i < j < N$, if

$$max(\frac{z_j - z_i}{j - i}) > tan(\theta_h) \tag{10}$$

where θ_h is the solar elevation angle. There is at least one point $j < N$ that can be connected to i to form a new slope so that the elevation angle of the new slope is greater than that of the sun. This indicates that point i cannot be irradiated; thus, $\Theta_i = 0$. Otherwise, $\Theta_i = 1$ (see Fig. 4).

(ii) For all $0 \leq i < i+1 < N$, let dS_i denote the slope consisting of the i-th and the $i+1$-th elevation values. If $\Theta_i = \Theta_{i+1} = 0$, dS_i is not irradiated at all; if $\Theta_i = \Theta_{i+1} = 1$, dS_i is fully irradiated, as shown in Fig. 3(a) and (b). Then, the irradiance formula can be expressed as:

$$E_i = E_{sun}\cos(\vec{N}, \vec{S}), \qquad when\ \Theta_i = \Theta_{i+1} = 1 \tag{11}$$

$$E_i = 0, \qquad when\ \Theta_i = \Theta_{i+1} = 1 \tag{12}$$

(iii) If $\Theta_i = 1, \Theta_{i+1} = 0$, then dS_i is partially irradiated, as shown in Fig. 3(c). The size of the irradiated area depends on the maximum occlusion point corresponding

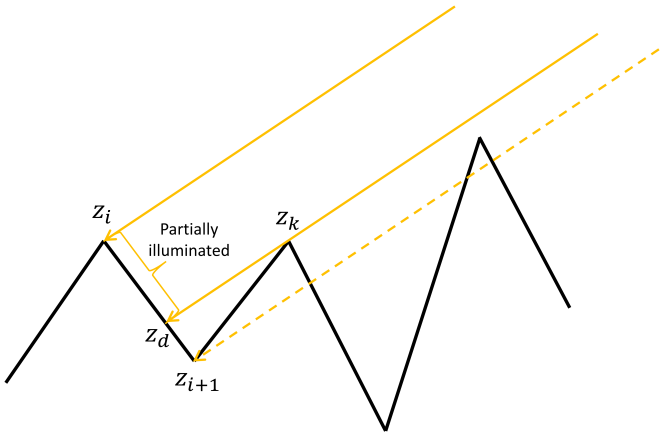

Fig. 5. A slope that is partially illuminated.

to z_{I+1} (denoted as z_k). The critical point at which the slope dS_i receives solar radiation can be obtained from the intersection of the line and $z_i z_{i+1}$ of solar rays passing through the point z_k (see Fig. 5). Assuming that the critical point is z_D, the irradiance formula for this irradiated area is:

$$E_i = \frac{|z_i\vec{z}_d|}{|z_i\vec{z}_{i+1}|}E_{sun}\cos(\vec{N}, \vec{S}), \qquad when\ \Theta_i = 1, \Theta_{i+1} = 0 \tag{13}$$

where E_{sun} is the direct solar irradiance, $\vec{N}$ is the normal to the terrain and $\vec{S}$ is the solar angle.

2) Incident irradiance of a two-dimensional terrain surface: Due to the irregular nature of the ground in rugged areas, the sky dome overlying a surface is not the integrated hemisphere of a horizontal surface [26]. Dozier [23] proposed determining the local horizon information from a grid. At any location, the portion of the overlying hemisphere that is obscured by terrain is:

$$\frac{1}{2\pi}\int_0^{2\pi} sin(h[\theta])d\theta \tag{14}$$

where $h[\theta]$ is the horizon angle in the direction θ. These horizons, however, are difficult to compute because, unlike slope and azimuth, they cannot be calculated from information restricted to the immediate neighborhood of a point.

By rotating a grid in direction ϕ_0, we reduce the horizon problem to its one-dimensional equivalent. Our interest is the angle to the horizon from any point in any direction, but we formulate the problem by determining the coordinates of the points that form the horizons. Minor errors in the elevation grid can therefore shift the "answer", i.e., the coordinates of the horizon point, by a considerable distance, but minor errors do not cause much variation in the end result, which is the angle to the horizon. When available digital terrain grids are sufficiently smooth, interpolation does not change the results [22].

A suitable interpolation method is selected for the rotation of the grid so that the relative azimuth of the incident solar ray is 0°. The rotation matrix of the grid is as follows:

(i) Forward rotation matrix:

$$\begin{pmatrix} x_1 \\ y_1 \\ 1 \end{pmatrix} = \begin{pmatrix} 1 & 0 & a_1 \\ 0 & 1 & b_1 \\ 0 & 0 & 1 \end{pmatrix} \begin{pmatrix} cos\phi_0 & sin\phi_0 & 0 \\ -sin\phi_0 & cos\phi_0 & 0 \\ 0 & 0 & 1 \end{pmatrix} \begin{pmatrix} 1 & 0 & -a_0 \\ 0 & 1 & -b_0 \\ 0 & 0 & 1 \end{pmatrix} \begin{pmatrix} x_0 \\ y_0 \\ 1 \end{pmatrix} \tag{15}$$

(ii) Inverse rotation matrix:

$$\begin{pmatrix} x_0 \\ y_0 \\ 1 \end{pmatrix} = \begin{pmatrix} 1 & 0 & -a_1 \\ 0 & 1 & -b_1 \\ 0 & 0 & 1 \end{pmatrix} \begin{pmatrix} cos\phi_0 & -sin\phi_0 & 0 \\ sin\phi_0 & cos\phi_0 & 0 \\ 0 & 0 & 1 \end{pmatrix} \begin{pmatrix} 1 & 0 & a_0 \\ 0 & 1 & b_0 \\ 0 & 0 & 1 \end{pmatrix} \begin{pmatrix} x_1 \\ y_1 \\ 1 \end{pmatrix} \tag{16}$$

(x_0, y_0) is the coordinate set before the grid rotation, and (x_1, y_1) is the coordinate set after the grid rotation. (a_0, b_0) and (a_1, b_1) are the coordinates of the center point before and after the grid rotation, respectively.

The rotated grid is calculated using the one-dimensional terrain surface incident irradiance method, and then the calculated matrix is rotated in the inverse direction of ϕ_0 to obtain the irradiance of the original grid.

It is assumed that the final solar direct incident irradiance is represented by matrix E_0, which can be written as:

$$E_0 = \begin{bmatrix} E_{11} & E_{12} & \cdots & E_{1c} \\ E_{21} & E_{22} & \cdots & E_{2c} \\ \vdots & \vdots & \ddots & \vdots \\ E_{r1} & E_{r2} & \cdots & E_{rc} \end{bmatrix} \tag{17}$$

E_{rc} represents the actual solar incident irradiance received by the grid points located in row r and column c.

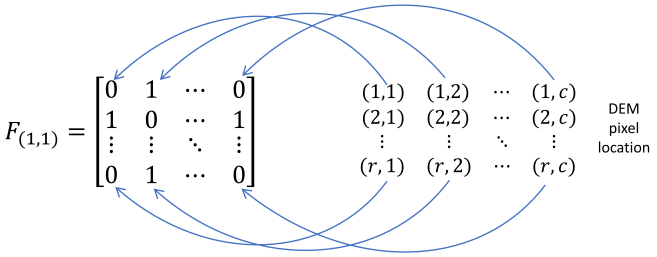

Fig. 6. A schematic diagram of the stored elements in the $F_{(1,1)}$ matrix corresponding to the position of the image.

C. Visible radiation factor between terrains

To quantify the magnitude of the new incident radiation on the surface of a microarea after each reflection, we need to determine in advance what other surfaces can reflect to the target. In this paper, the mutual reflection between surfaces is reduced to the mutual visibility between grid points. For a given terrain, the mutual reflection relationship between any slope pair is also certain. We first calculate whether there is a reflection between any two slopes. The binary matrix $F_{(r,c)}$ stores the reflection relations between the grid point at position (r, c) and all other slope points, and the matrix elements are 0 or 1. As shown in the figure, $F_{(1,1)}$ is used as an example:

When $F_{(1,1)}(1,1) = 0$, the DEM pixel at position $(1,1)$ in the grid matrix includes no self-reflection; when $F_{(1,1)}(1,2) = 1$, reflection occurs between DEM pixels at position $(1,2)$ and pixels at position $(1,1)$.

We fit the elevation value of the "position" on the linear path between the "radiation source point" and the "target receiving point" by the adjacent point values and determine whether the radiation rays are "blocked", as shown in Fig. 7. As seen from the figure, there are not always true elevation points on the radiating paths of $A \to B$ and $A \to C$ (there are no elevation points at the double circle in the figure). We define the position of the elevation value pass on the radiation path between the radiation source and the target receiving point as the "intermediate slope point" (the intermediate slope point may or may not be present in an image). The number of intermediate slope points depends on the maximum distance between the radiation source and the target receiver in the *row* and *col* directions.

The $Oxyz$ spatial Cartesian coordinate system is established, where x and y correspond to the row value and column value of the DEM image, respectively, and the unit interval is equal to the spatial resolution of the DEM, set as t. The size of z is the ratio of the elevation value to the spatial resolution. Therefore, the units of x, y, and z are unified, i.e., $(t \cdot m/pixel)$. For any two points $A(x_a, y_a, z_a)$ and $B(x_b, y_b, z_b)$ in $Oxyz$,

(i) For $max(|x_a - x_b|, |y_a - y_b|) = 1$, the number of intermediate slope points is $num = 0$; that is, points A and B are adjacent, AB forms a slope, and there is no

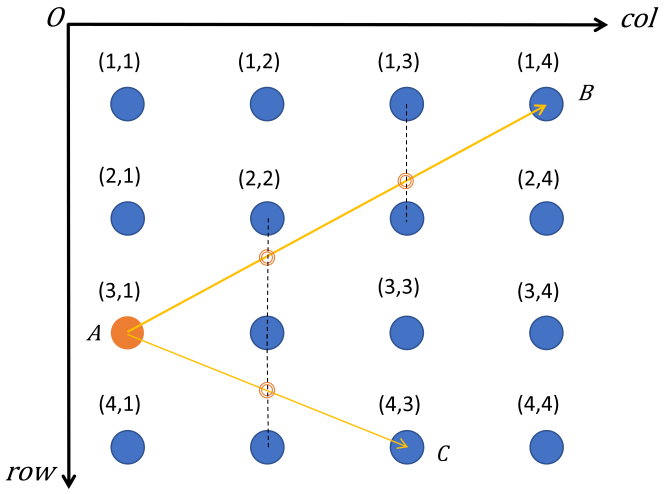

Fig. 7. A diagram of the actual position of the elevation value on the radiation path. A is the radiation source, and B and C are the target receiving points. The yellow line is the radiation emitted by A. The double circles are the actual elevation positions on the radiation path.

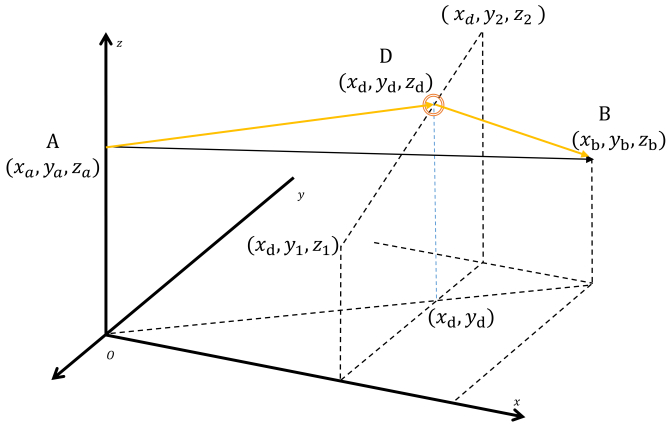

Fig. 8. The actual position and elevation of the intermediate slope point

reflection for AB.

(ii) For $max(|x_a - x_b|, |y_a - y_b|) > 1$, if $|x_a - x_b| > |y_a - y_b|$, the number of intermediate slope points is $num = |x_a - x_b| - 1$. Let the intermediate slope point be $D(x_d, y_d, z_d)$. For $x_a < x_d < x_b$, y_d is the intersection of the perpendicular of $(x_d, 0)$ in the direction of y and the projection of AB in the two-dimensional plane of Oxy. $y1 = floor(y_d)$, and $y2 = ceil(y_d)$, where $z1$ is the elevation value of $(x_d, y1)$ and $z2$ is the elevation value of $(x_d, y2)$ (see Fig. 8). Then, the formula for z_d is:

$$z_d = z_1 + \frac{y_d - y_1}{y2 - y1}(z_2 - z_1) \tag{18}$$

(iii) For $max(|x_a - x_b|, |y_a - y_b|) > 1$, if $|x_a - x_b| < |y_a - y_b|$, the number of intermediate slope points is $num = |y_a - y_b| - 1$. Let the intermediate slope point be $D(x_d, y_d, z_d)$. For $y_a < y_d < y_b$, x_d is the intersection of the perpendicular of $(0, y_d)$ in the direction of x and the projection of AB in the two-dimensional plane of Oxy. $x1 = floot(x_d)$, and $x2 = ceil(x_d)$, where $z1$ is the elevation value of (x_1, y_d) and $z2$ is the elevation value of $(x2, y_d)$. Then, the formula for z_d is:

$$z_d = z_1 + \frac{x_d - x_1}{x2 - x1}(z_2 - z_1) \tag{19}$$

Therefore, it is possible to calculate whether any point D on the "radiation path" of AB occludes AB. The judgment process is similar to that expressed in formula (10). Alternatively, this judgement can be based on the position of z_d (i.e., whether z_d is above or below line AB).

Based on the binary matrix F of each pixel position, the visible radiation factor Γ of terrain corresponding to each pixel position can be obtained by combining the formula (6).

D. Matrix representation of multiple reflections between terrains

According to the content in the previous three sections, we express the multiple-reflection process between terrains in the form of a matrix. The reflectance of the microtopography is assumed to be ρ, and Lambert reflection is considered. Let the matrix T_n store the incident irradiance on the surface of each DEM pixel of the nth-order; then:

$$T_1 = E_0 = \begin{bmatrix} E_{11} & E_{12} & \cdots & E_{1c} \\ E_{21} & E_{22} & \cdots & E_{2c} \\ \vdots & \vdots & \ddots & \vdots \\ E_{r1} & E_{r2} & \cdots & E_{rc} \end{bmatrix}, \qquad n = 1 \tag{20}$$

$$T_n = \rho^{n-1} \cdot \begin{bmatrix} sum(T_{n-1} \odot \Gamma_{(1,1)}) & sum(T_{n-1} \odot \Gamma_{(1,2)}) & \cdots & sum(T_{n-1} \odot \Gamma_{(1,c)}) \\ sum(T_{n-1} \odot \Gamma_{(2,1)}) & sum(T_{n-1} \odot \Gamma_{(2,2)}) & \cdots & sum(T_{n-1} \odot \Gamma_{(2,c)}) \\ \vdots & \vdots & \ddots & \vdots \\ sum(T_{n-1} \odot \Gamma_{(r,1)}) & sum(T_{n-1} \odot \Gamma_{(r,2)}) & \cdots & sum(T_{n-1} \odot \Gamma_{(r,c)}) \end{bmatrix}, \qquad n > 1 \tag{21}$$

$T_{n-1} \odot \Gamma_{(r,c)}$ represents the multiplication of each element in the corresponding position of matrix T_{n-1} and matrix $\Gamma(r, c)$, resulting in a matrix of the same size. $sum(T_{n-1} \odot \Gamma_{(r,c)})$ denotes adding all the elements of the resulting matrix.

Each element in T_n gradually tends to 0 over multiple radiative reflections. The final total reflected radiance of the whole DEM image to the sky L_{ref} can be expressed

as:

$$L_{ref} = \frac{\rho}{\pi}(T_1 + T_2 + \cdots + T_n) \tag{22}$$

E. The total reflected radiance in the observed direction

It is assumed that the illumination of each microarea at the incident angle is given by matrix B_s and that the visibility of each microarea at the observation angle is given by matrix B_v. According to the principle of reciprocity of angles, $B_s = B_v$ at the same angle.

Therefore, assuming that incident radiation from the observation direction irradiance is 1 $W \cdot m^{-2}$. According to the aforementioned calculation method of actual incident irradiance on the surface, if in the observation direction the irradiance on the surface is greater than zero, then the surface can be "observed". These areas are set to 1 in the matrix B_v, and others are set to 0. Then, the binary visibility matrix B_v is obtained, such as:

$$B_v = \begin{bmatrix} b_{11} & b_{12} & \cdots & b_{1c} \\ b_{21} & b_{22} & \cdots & b_{2c} \\ \vdots & \vdots & \ddots & \vdots \\ b_{r1} & b_{r2} & \cdots & b_{rc} \end{bmatrix} \tag{23}$$

where $b_{rc} = 0$ or $b_{rc} = 1$. In the process of obtaining B_v, the relative observation angle matrix i_v of each slope in the observation direction can also be obtained.

Then, the reflected radiance L_v in a specific observation direction can be expressed as:

$$L_v = L_{ref} \odot cos(i_v) \tag{24}$$

F. Remote sensing pixel reflectance and actual terrain reflectance

Considering the effect of microtopography in a single remote-sensing observation pixel, the reflectance of microtopography is assumed to be ρ, and Lambert reflection is considered. The reflectivity of a single remote-sensing observation pixel is ρ_v.

Let $T_n = \rho^{n-1} \cdot D_{n-1}, (n > 2)$. D_{n-1} represents the $n-1$th reflection effect between terrains. When $n = 1$, $D_0 = T_1 = E_0$. Therefore,

$$L_{ref} = \frac{\rho}{\pi}(T_1 + T_2 + \cdots + T_n) = \frac{\rho D_0 + \rho^2 D_1 + \cdots + \rho^n D_{n-1}}{\pi} \tag{25}$$

It is assumed that the observation angle is (θ_v, φ_v), where θ_v is the observation zenith and φ_v is the observation azimuth. Then, according to the observed radiance:

$$\rho_v \frac{E_{sun} cos(\theta_0)}{\pi} \cdot cos(\theta_v) = \frac{\rho D_0 + \rho^2 D_1 + \cdots + \rho^n D_{n-1}}{\pi} \odot cos(i_v) \tag{26}$$

where E_{sun} is the direct solar irradiance and θ_0 is the solar zenith. When the topography is completely horizontally flat, there is only one reflection from the terrain surface. Therefore, $D_0 = E_{sun} cos(\theta_0)$, $\theta_v = i_v$, and $\rho = \rho_v$.

Formula (26) shows that the observation-based reflectance of low-spatial-resolution remote sensing pixels is a function of the real reflectance of the microtopography inside the pixel, terrain roughness, solar incidence angle, and remote sensing observation angle. The influencing factors are the initial incident irradiance of the terrain surface under solar illumination, multiple reflection effects caused by terrain undulation, and observation masking.

III. Data

A. Simulated DEM

A simulated DEM with 50×50 grid cells was generated with the "normrnd" function in MATLAB. Each grid cell and the mean elevation were assumed to be 1 unit, and the standard elevation error was 0.25 units. DEMs with different slopes could be simulated by appropriately exaggerating the vertical elevation and fixing the grid cell size. For this research, the vertical elevation was multiplied separately by factors of 1, 10, and 20, and a moving average filter was applied to smooth the exaggerated data to form a simulated DEM that closely represents the actual undulating topography of the Moon. The filter templates were 55, 77, and 99 units. Nine simulated DEMs were generated (see Fig. 9), and the statistical mean slopes are listed in Table I.

TABLE I
Average slopes of the nine simulated DEMs

	Average slope (°)		
Filter	Exaggeration = 1	Exaggeration = 10	Exaggeration = 20
55	1.5418	14.7462	26.7780
77	0.9063	8.6374	17.8266
99	0.6379	6.4140	12.3107

B. Real data

1) Chang'e-3 landing site: The Chang'e-3 landing site is located at $(44.1205°N, 19.5102°W)$ [27], and a large area around the landing site has a homogeneous composition. Compared to the MS-2, Apollo 15, and Apollo 16 highland sites, the CE-3 site is much younger and less impacted and contaminated [28]. In this paper, the CE-3 landing site is selected as the center, and the site is considered to expand approximately 1800 m in four directions (east, west, north, and south), forming an area with a size of approximately 3600×3600 m^2 (see Table II). The new model is applied to the area for further analysis. In addition, the in situ spectral radiance and reflectance factor (REFF) measured

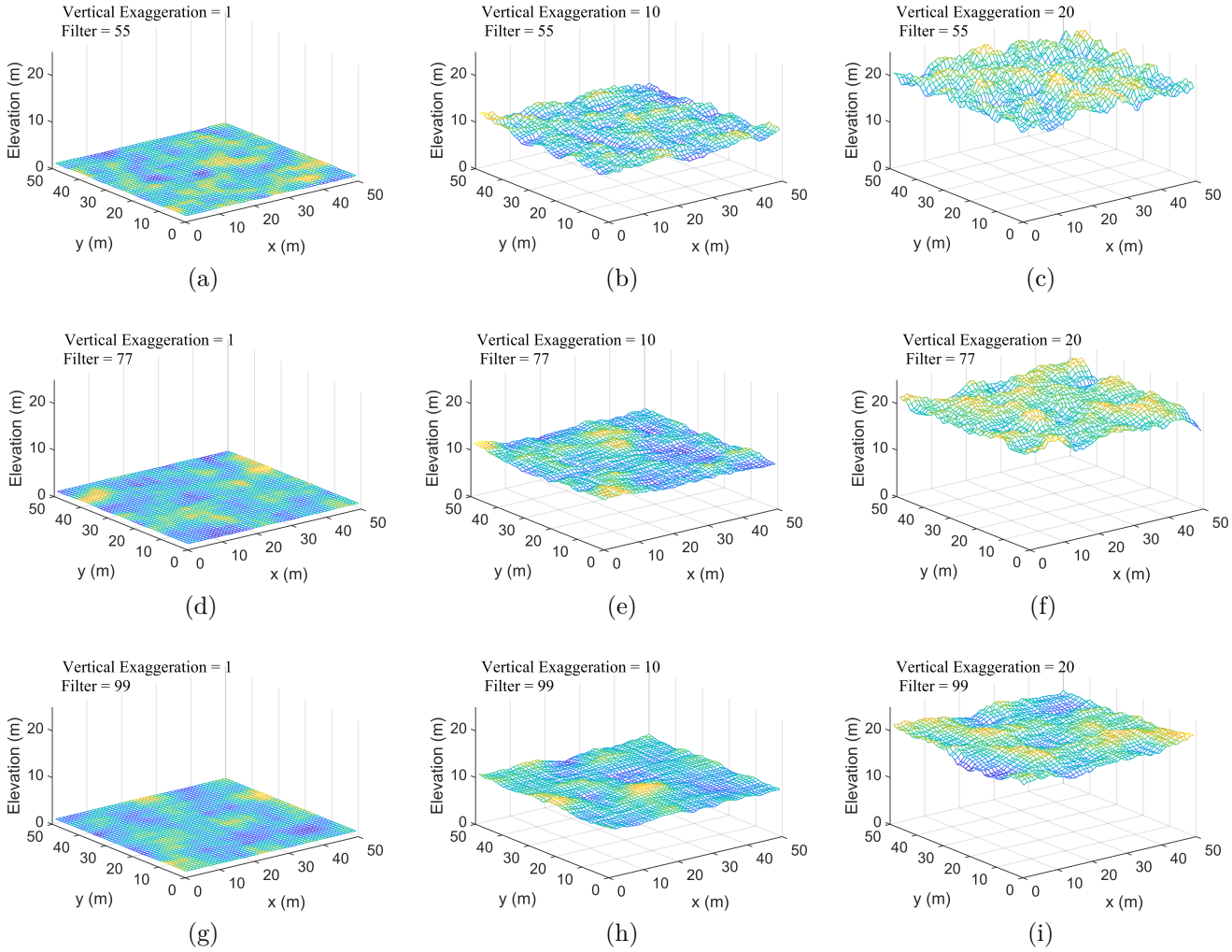

Fig. 9. Schematic diagram of the nine simulated DEMs with different topographic undulations.

by VNIS on the CE-3 "Yutu" detector are given in the paper of [28] (here, we choose a wavelength range of 450 − 1000 nm). The data are also used as a standard to verify the accuracy of the new model.

2) LOLA DEM data: The DEM data used in this paper were collected by LOLA aboard the LRO launched by the United States on June 19, 2009. The spatial resolution of the data is approximately 60 m, and the data can be obtained at http://imbrium.mit.edu. Because DEM imagery has obvious stripes, the images were preprocessed. As shown in Fig. 10, the processed image displays a good visual transition. Fig. 11 shows the 3D topographic map of the area from an azimuth view of 135° and an elevation angle of 45°.

TABLE II
Basic parameters of the real DEM from LOLA

Parameter	DEM
Center location	$44.1205°N, 19.5102°W$
Number of pixels	60×60
Actual area size	$3600 \times 3600\ m^2$
Maximum elevation value	-2683
Minimum elevation value	-2622
Terrain spatial resolution	$\sim 60m$
Average slope	1.0198°

IV. Results

A. Analysis of the simulation experiment results

1) Comparative analysis of the directional radiance for the first reflection and multiple reflections: Given that the solar incident angle is $(30°, 0°)$, the observation angle is $(0°, 0°)$, and the direct solar incident irradiance is $100\ W \cdot m^{-2}$, it is assumed that the reflectance of each microarea in the simulated DEM is equal and Lambertian, with reflectance $\rho = 0.03$. DEM data with an average slope of 17.8266° (see Fig. 9(f)) were selected to analyze the directional radiance for the first reflection and multiple reflections. According to the theory introduced in this paper, the result of the first reflection is the result of the reflection of adjacent terrains in the Proy model. The results are shown in Fig. 12.

Fig. 12 shows the total radiance of reflection increases

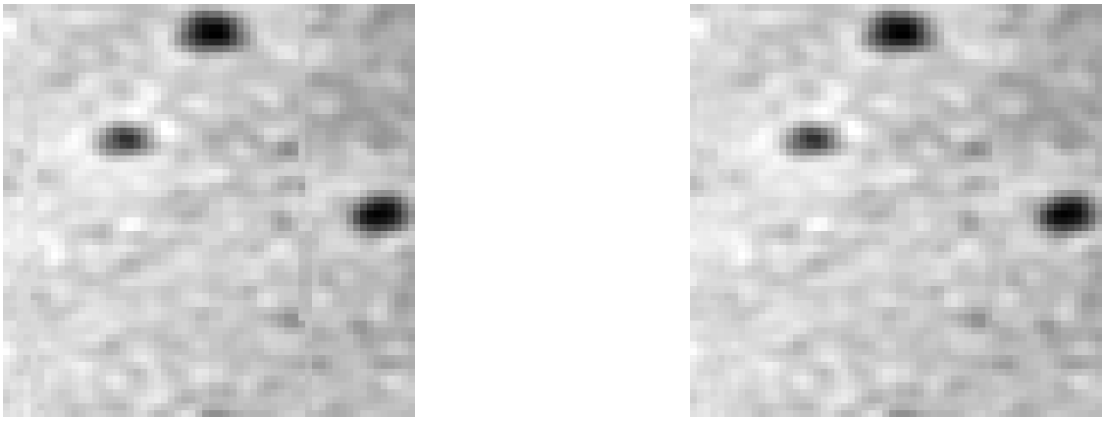

(a) (b)

Fig. 10. DEM area display and image preprocessing results. (a) The original image; (b) the processed images.

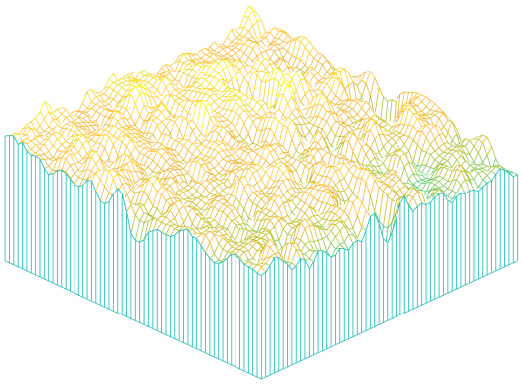

Fig. 11. A three-dimensional schematic of the DEM image from an azimuth view of 135° and an elevation angle of 45°.

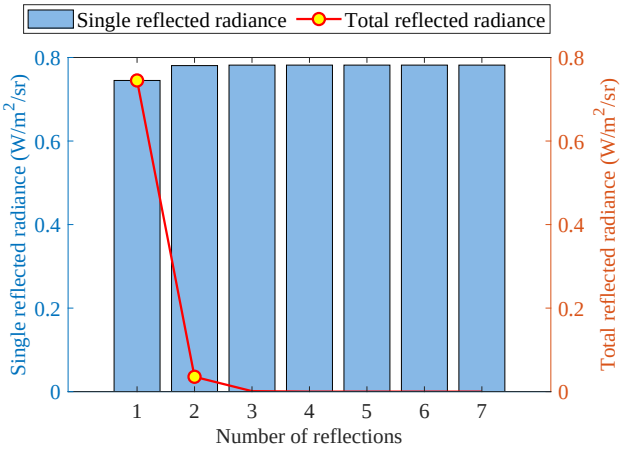

Fig. 12. Diagram comparing the single- and multiple-reflection results. The bar represents the sum of each reflection and all previous reflections, and the line connects the results for each single-reflection.

gradually with the number of reflections, and the result of each reflection decreases from large to small and approaches zero. Among them, the first and second reflections account for the greatest proportions of the total reflection. According to the data in Table III, the radiance of multiple reflections increases by approximately 4.9% based on the first reflection.

The percentage increases in total reflected radiance compared to the first reflected radiance of nine groups of terrains were calculated, and the results are shown in Table IV.

2) Overall directional reflectance of different landforms: In this case, the parameter settings are the same as those above. According to the microarea reflectance $\rho = 0.03$, we calculated the overall directional reflectance based on nine DEMs, as shown in Table V.

Fig. 13 shows that when the topography is relatively flat, the overall directional reflectance is close to that of completely flat areas (i.e., 0.03) but slightly greater than that of completely flat areas. With the increase in the average slope of the terrain, the overall directional reflectance gradually decreases and is less than 0.03. This is because the reflection of the surrounding terrain in-

TABLE III
Single reflected radiance and total reflected radiance for Fig.9(f)
(Unit: $W \cdot m^{-2} \cdot sr^{-1}$)

Number of reflections	Single reflected radiance	Total reflected radiance
1	0.745030159	0.745030159
2	0.035568553	0.780598712
3	0.001157863	0.781756575
4	3.06E-05	0.781787201
5	7.76E-07	0.781787977
6	3.53E-09	0.781787981
7	0	0.781787981

TABLE IV
Percentage increase in total reflected radiance compared to the first reflected radiance

Average slope (°)	0.6379	0.9063	1.5418	6.4140	8.6374	12.3107	14.7462	17.8266	26.7780
Percentage increase (%)	6.04	5.26	4.73	6.21	5.08	5.45	4.72	4.93	4.73

TABLE V
Overall directional reflectance of nine DEMs

Average slope (°)	0.6379	0.9063	1.5418	6.4140	8.6374	12.3107	14.7462	17.8266	26.7780
Reflectance	0.0318	0.0316	0.0314	0.0314	0.0307	0.0297	0.0290	0.0284	0.0245

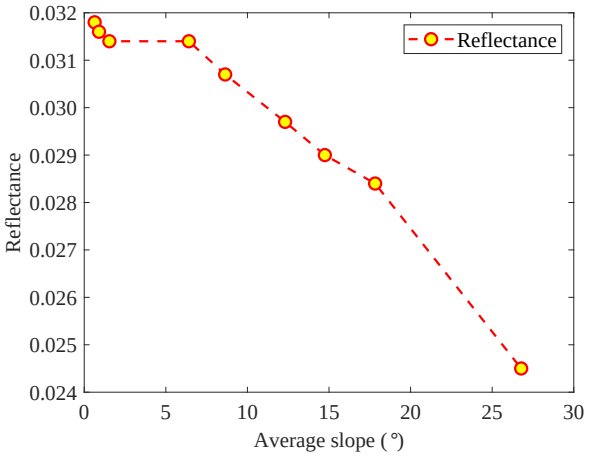

Fig. 13. Schematic diagram of the overall directional reflectance of nine DEMs.

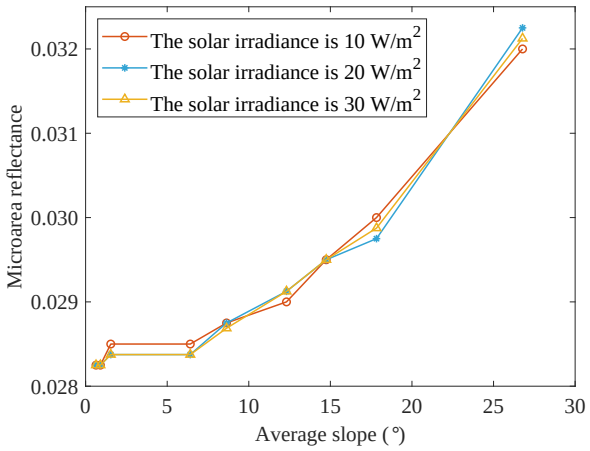

Fig. 14. The retrieved results of microarea reflectance for nine DEMs.

creases the incident irradiance of the terrain surface, which increases the final radiance reflected in the direction of observation. As the average slope of the terrain increases, the terrain becomes steeper, and more shadows are created through shielding. This process reduces the initial solar direct incident irradiance of the terrain surface, resulting in a reduction in the radiation that circulates during the inner terrain reflection process. Therefore, the overall directional reflected radiance is reduced, which leads to a decrease in overall directional reflectance.

3) Reflectance inversion of a microarea under the same observed reflected radiance: It is assumed that the terrain is completely flat with $\rho = 0.03$ and the direct solar incident irradiance is 10, 20, and 30 $W \cdot m^{-2}$, therefore, the observed radiances are 0.0827, 0.1654, and 0.2481 $W \cdot m^{-2} \cdot sr^{-1}$, respectively. The other parameters are the same as those in the previous section. With incident irradiance and reflected radiance for flat terrain as controls, we invert the microarea reflectance for nine simulated DEMs. The results are shown in Fig. 14.

Fig. 14 shows that under the same illumination observation conditions, if the observed reflected radiances are equal, as the average slope of the terrain increases, the inversion reflection of the microarea will initially be less than 0.03 and then gradually increase to more than 0.03. The reason why the reflectivity is less than 0.03 is that the reflection of adjacent terrain increases the irradiance on the terrain surface when the topography relief degree is low. As the average slope increases, the undulating terrain reduces the incident irradiance on the slope surface, and the multiple reflections between terrains consume more radiation energy. Therefore, only the reflectivity of the microarea is large enough (like a lager than 0.03) to offset these energy losses to obtain the same observed radiance. Moreover, the difference in solar incident irradiance has a certain influence on the inversion results of reflectivity.

From the above results, it can be concluded that the decrease in incident irradiance caused by rugged terrain and the increase in irradiance caused by adjacent terrain are two mutually restricting factors. The reflected radiance of the actual terrain is closely related to the degree of relief of the terrain.

B. Comparison of the reflectance obtained from the new model and the Chang'e-3 in situ measurement reflectance

Fig. 15 shows the reflectivity obtained with the new model based on spectral radiance data observed at the Chang'e-3 landing site. The model inversion reflectance cruve is very similar to the in situ measured reflectance curve provided in the literature (see appendix A for specific data). If the in situ measured reflectance data are considered the true values, the relative error of model

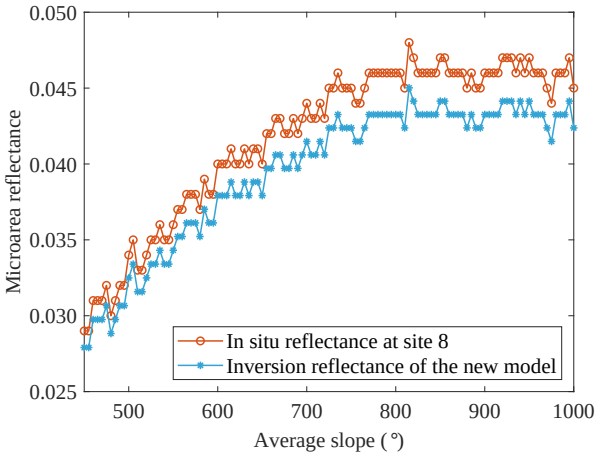

Fig. 15. Comparison of the reflectance obtained from the new model and the Chang'e-3 in situ measurement reflectance

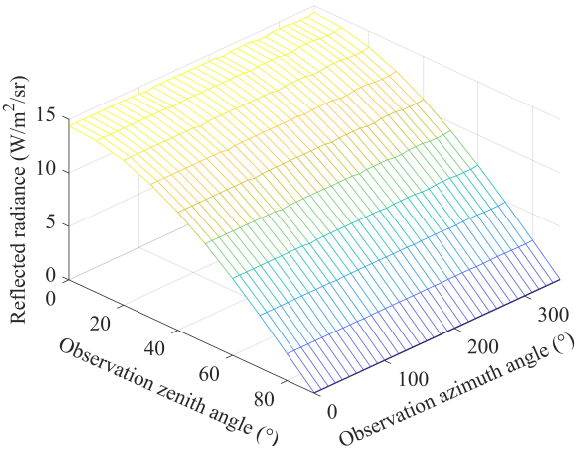

Fig. 16. The radiance in each observation direction at 450 nm considering the reflectance of the microarea is 0.029.

inversion is between −3.7% and −6.3%. The results demonstrate the accuracy of the new model.

Therefore, the new model can be used to calculate the radiance under other illumination observation geometries based on the reflectance values in the literature. The results are shown in Fig. 16, with the reflectance at a wavelength of 450 nm being 0.029.

Fig. 16 shows that the radiance curves for each azimuth angle are basically flat at the same zenith angle. At the same azimuth angle, with increasing observation zenith angle, the reflected radiance gradually decreases.

The experimental results show that the area is characterized by generally uniform reflection characteristics.

V. Conclusion

The stable luminosity of the lunar surface makes the Moon an ideal external calibration source for spaceborne remote sensing instruments. Lunar calibration techniques have been widely developed for solar reflective bands. Currently, the ROLO model with the highest calibration accuracy in the world still has an uncertainty of 5–10%. Zhang et al. [3] and Sun et al. [4] improved the model accuracy based on ROLO model parameters such as reflectivity and irradiance data. Wu et al. [6] established a lunar irradiance model based on lunar satellite data. Nevertheless, the albedos of mare and highlands are very different, and the relationship between the albedos change and the observation geometry varies. A modeling method based on the global irradiance/reflected radiance of the Moon is bound to result in higher uncertainty. With the improvement of the spatial resolution of remote sensing instruments, the local radiance of the Moon can be more easily observed for calibration. However, large and small impact craters are densely distributed on the lunar surface [7]. At the meter to hectometer scales, there are obvious differences in the median bidirectional slope, RMS height, and median absolute slope between mares and highlands [8]. Rugged terrain often alters illumination and viewing geometry and generates relief shadows, observation masking, and multiple scattering, resulting in intense topographic dependence on the total incident and reflected radiance [9]–[11]. If a local area on the Moon is used for calibration, the topographic effect should be considered.

In this paper, a new model for quantifying multiple reflections of radiation between terrains is presented. Based on the adjacent terrain irradiance formula of the first-order reflection proposed by Proy, the second-order to the *nth*-order reflections of radiation between terrains are derived. Moreover, the expression of the quantitative relationships among the incident irradiance of each surface and the number of reflections of radiation between terrains, and the number of mutually visible slopes is established. It is concluded that the observation-based reflectance of low-spatial-resolution remote sensing pixels is a function of the real reflectance of the microtopography inside the pixel, terrain roughness, solar incidence angle, and remote sensing observation angle (see formula (26)). The influencing factors are the initial incident irradiance of the terrain surface under solar illumination, multiple reflection effects caused by terrain undulation, and observation masking.

Simulation experiments show that for the same illumination observation geometry, the radiance after multiple reflections is often several percentage points higher than that after one reflection. We believe that this difference should not be overlooked. In addition, slightly undulating terrain will increase the overall directional reflected radiance, but when the topography is undulating, the overall directional reflected radiance will decrease gradually. When there are different degrees of topography relief in the same size areas, if the observed directional reflected radiances are equal under the same illumination observation geometry, the inversion reflectance of the microtopography will vary due to differences in landscape. In general, the higher the degree of terrain undulation is, the higher the reflectivity of the microtopography surface. In addition, solar incident irradiance has a certain influence on reflectivity.

For the actual terrain data, we selected LOLA data, and for the actual radiance data and reflectivity data, we selected the in situ measurements from the Chang'e-3 landing site (the selected wavelength ranged from 450 nm to 1000 nm). The experimental results showed that the reflectance curve of the new model was very similar to that based on the Chang'e-3 data, and the relative error of the results was between -3.7% and -6.3%. This finding proves the accuracy of the new model. In addition, we calculated the overall reflected radiance in each observation direction under the same illumination conditions by using the reflectance of the 450 nm wavelength from in situ Chang'e-3 measurements. The results showed that the radiance curves of all observed azimuth angles exhibit good consistency at the same observation zenith angle. At the same observation azimuth, the reflected radiance decreases with increasing observation zenith angle. The experimental results indicate that the study area is characterized by relatively uniform reflection.

Compared with previous terrain correction models and photometric correction models, the proposed model can quantify the "contribution" of radiation to the surface irradiance of terrain after each reflection. And the experimental results verify that the radiance of multiple reflections increases by several percentage points compared with that of the first reflection. This finding highlights the importance of considering multiple reflections of radiation between terrains when retrieving the true reflectance of terrains. The research results in this paper can aid in correcting the reflectance values of remote sensing pixels and provide important reference significance for the construction of surface BRDF.

Appendix A
The in situ reflectance at site 8 and the inversion results of the new model

Appendix A comprises Table A1.

References

[1] T. Stone and H. Kieffer, "Assessment of uncertainty in ROLO lunar irradiance for on-orbit calibration," SPIE Proceedings, vol. 5542, 2004,10,26.

[2] Aimé Meygret, Gwendoline Blanchet, Stéphane Colzy, and Lydwine Gross-Colzy, "Improving ROLO lunar albedo model using PLEIADES-HR satellites extra-terrestrial observations," in Earth Observing Systems XXII, vol. 10402, 2017,9,5.

[3] L. Zhang, P. Zhang, X. Q. Hu, L. Chen, and M. Min, "A novel hyperspectral lunar irradiance model based on ROLO and mean equigonal albedo," Optik, vol. 142, pp. 657–664, 2017,8.

[4] J. Sun and X. Xiong, "Improved Lunar Irradiance Model Using Multiyear MODIS Lunar Observations," IEEE Transactions on Geoscience and Remote Sensing, vol. 59, no. 6, pp. 5154–5170, 2021,6.

[5] J. D. Goguen, T. C. Stone, H. H. Kieffer, and B. J. Buratti, "A new look at photometry of the Moon," Icarus, vol. 208, no. 2, pp. 548–557, 2010,8.

[6] Y. Wu, X. Hu, and S. Li, "The Irradiance Model of the Moon and Its Implication on the On-orbit Calibration of Spacecraft," in The 4th Annual Conference on High Resolution Earth Observation, 2017, p. 9.

[7] R. Jaumann, H. Hiesinger, M. Anand, I. A. Crawford, R. Wagner, F. Sohl, B. L. Jolliff, F. Scholten, M. Knapmeyer, H. Hoffmann, H. Hussmann, M. Grott, S. Hempel, U. Köhler, K. Krohn, N. Schmitz, J. Carpenter, M. Wieczorek, T. Spohn, M. S. Robinson, and J. Oberst, "Geology, geochemistry, and geophysics of the Moon: Status of current understanding," Planetary and Space Science, vol. 74, no. 1, pp. 15–41, 2012,12.

[8] Y. Z. Cai and W. Z. Fa, "Meter-Scale Topographic Roughness of the Moon: The Effect of Small Impact Craters," Journal of Geophysical Research: Planets, vol. 125, no. 8, p. 24, 2020,8.

[9] C. B. Schaaf, L. Xiaowen, and A. H. Strahler, "Topographic effects on bidirectional and hemispherical reflectances calculated with a geometric-optical canopy model," IEEE Transactions on Geoscience and Remote Sensing, vol. 32, no. 6, pp. 1186–1193, 1994.

[10] J. Wen, X. Zhao, Q. Liu, Y. Tang, and B. Dou, "An Improved Land-Surface Albedo Algorithm With DEM in Rugged Terrain," IEEE Geoscience and Remote Sensing Letters, vol. 11, no. 4, pp. 883–887, 2014,4.

[11] J. Wen, Q. Liu, Q. Xiao, Q. Liu, D. You, D. Hao, S. Wu, and X. Lin, "Characterizing Land Surface Anisotropic Reflectance over Rugged Terrain: A Review of Concepts and Recent Developments," Remote Sensing, vol. 10, no. 3, p. 370, 2018.

[12] J. Zhang, Z. Ling, W. Zhang, X. Ren, C. Li, and J. Liu, "Photometric modeling of the Moon using Lommel-Seeliger function and Chang'E-1 IIM data," Chinese Science Bulletin, vol. 58, no. 36, pp. 4588–4592, 2013,12.

[13] S. B. Chen, J. R. Wang, P. J. Guo, and M. C. Wang, "Sandmeier Model Based Topographic Correction to Lunar Spectral Profiler (SP) Data from KAGUYA Satellite," Spectroscopy and Spectral Analysis, vol. 34, no. 9, pp. 2573–2577, Sep. 2014.

[14] X. S. Xu, J. J. Liu, D. W. Liu, B. Liu, and R. Shu, "Photometric Correction of Chang'E-1 Interference Imaging Spectrometer's (IIM) Limited Observing Geometries Data with Hapke Model," Remote Sensing, vol. 12, no. 22, p. 3676, Nov. 2020.

[15] X. Lin, J. Wen, S. Wu, D. Hao, Q. Xiao, and Q. Liu, "Advances in topographic correction methods for optical remote sensing imageries," Journal of Remote Sensing, vol. 24, no. 8, pp. 958–974, 2020.

[16] S. A. Soenen, D. R. Peddle, and C. A. Coburn, "SCS+C: A modified sun-canopy-sensor topographic correction in forested terrain," IEEE Transactions on Geoscience and Remote Sensing, vol. 43, no. 9, pp. 2148–2159, 2005,9.

[17] B. W. Hapke, "A theoretical photometric function for the lunar surface," JOURNAL OF GEOPHYSICAL RESEARCH, vol. 68, no. 15, pp. 279–280, 1963.

[18] B. Hapke, "Bidirectional reflectance spectroscopy: 1. Theory," Journal of Geophysical Research: Solid Earth, vol. 86, no. B4, pp. 3039–3054, 1981,4,10.

[19] B. Hapke, "An improved theoretical lunar photometric function," The Astronomical Journal, vol. 71, no. 5, p. 386, 1966.

[20] B. Hapke, Theory of Reflectance and Emittance Spectroscopy, 2012, vol. 47.

[21] C. Proy, D. Tanré, and P. Y. Deschamps, "Evaluation of topographic effects in remotely sensed data," Remote Sensing of Environment, vol. 30, no. 1, pp. 21–32, 1989,10.

[22] J. Dozier, J. Bruno, and P. Downey, "A faster solution to the horizon problem," Computers & Geosciences, vol. 7, no. 2, pp. 145–151, 1981,1.

[23] J. Dozier and J. Frew, "Rapid calculation of terrain parameters for radiation modeling from digital elevation data," IEEE Transactions on Geoscience and Remote Sensing, vol. 28, no. 5, pp. 963–969, 1990.

[24] S. Sandmeier and K. I. J. G. Itten, "A physically-based model to correct atmospheric and illumination effects in optical satellite data of rugged terrain," IEEE Transactions on Geoscience and Remote Sensing, vol. 35, no. 3, pp. 708–717, 1997.

[25] H. Li, L. Xu, H. Shen, and L. Zhang, "A general variational framework considering cast shadows for the topographic correction of remote sensing imagery," ISPRS Journal of Photogrammetry and Remote Sensing, vol. 117, pp. 161–171, 2016,7.

[26] J. Wen, Q. Liu, Y. Tang, B. Dou, D. You, Q. Xiao, Q. Liu, and X. Li, "Modeling Land Surface Reflectance Coupled BRDF for HJ-1/CCD Data of Rugged Terrain in Heihe River Basin, China," IEEE Journal of Selected Topics in Applied Earth Observations and Remote Sensing, vol. 8, no. 4, pp. 1506–1518, 2015,4.

TABLE A1
The in situ reflectance at site 8 and the inversion results of the new model

Wavelength (nm)	Reflectance	The inversion results	The relative error (%)	Wavelength (nm)	Reflectance	The inversion results	The relative error (%)
450	0.029	0.02790625	-3.77	730	0.045	0.04237500	-5.83
455	0.029	0.02790625	-3.77	735	0.046	0.04325781	-5.96
460	0.031	0.02975000	-4.03	740	0.045	0.04237500	-5.83
465	0.031	0.02975000	-4.03	745	0.045	0.04237500	-5.83
470	0.031	0.02975000	-4.03	750	0.045	0.04237500	-5.83
475	0.032	0.03066406	-4.17	755	0.044	0.04148438	-5.72
480	0.030	0.02882813	-3.91	760	0.044	0.04148438	-5.72
485	0.031	0.02975000	-4.03	765	0.045	0.04237500	-5.83
490	0.032	0.03066406	-4.17	770	0.046	0.04325781	-5.96
495	0.032	0.03066406	-4.17	775	0.046	0.04325781	-5.96
500	0.034	0.03249219	-4.43	780	0.046	0.04325781	-5.96
505	0.035	0.03340234	-4.56	785	0.046	0.04325781	-5.96
510	0.033	0.03158203	-4.30	790	0.046	0.04325781	-5.96
515	0.033	0.03158203	-4.30	795	0.046	0.04325781	-5.96
520	0.034	0.03249219	-4.43	800	0.046	0.04325781	-5.96
525	0.035	0.03340234	-4.56	805	0.046	0.04325781	-5.96
530	0.035	0.03340234	-4.56	810	0.045	0.04237500	-5.83
535	0.036	0.03431250	-4.69	815	0.048	0.04501563	-6.22
540	0.035	0.03340234	-4.56	820	0.047	0.04414063	-6.08
545	0.035	0.03340234	-4.56	825	0.046	0.04325781	-5.96
550	0.036	0.03431250	-4.69	830	0.046	0.04325781	-5.96
555	0.037	0.03521875	-4.81	835	0.046	0.04325781	-5.96
560	0.037	0.03521875	-4.81	840	0.046	0.04325781	-5.96
565	0.038	0.03611719	-4.95	845	0.046	0.04325781	-5.96
570	0.038	0.03611719	-4.95	850	0.047	0.04414063	-6.08
575	0.038	0.03611719	-4.95	855	0.047	0.04414063	-6.08
580	0.037	0.03521875	-4.81	860	0.046	0.04325781	-5.96
585	0.039	0.03701953	-5.08	865	0.046	0.04325781	-5.96
590	0.038	0.03611719	-4.95	870	0.046	0.04325781	-5.96
595	0.038	0.03611719	-4.95	875	0.046	0.04325781	-5.96
600	0.040	0.03791797	-5.21	880	0.045	0.04237500	-5.83
605	0.040	0.03791797	-5.21	885	0.046	0.04325781	-5.96
610	0.040	0.03791797	-5.21	890	0.045	0.04237500	-5.83
615	0.041	0.03881250	-5.34	895	0.045	0.04237500	-5.83
620	0.040	0.03791797	-5.21	900	0.046	0.04325781	-5.96
625	0.040	0.03791797	-5.21	905	0.046	0.04325781	-5.96
630	0.041	0.03881250	-5.34	910	0.046	0.04325781	-5.96
635	0.040	0.03791797	-5.21	915	0.046	0.04325781	-5.96
640	0.041	0.03881250	-5.34	920	0.047	0.04414063	-6.08
645	0.041	0.03881250	-5.34	925	0.047	0.04414063	-6.08
650	0.040	0.03791797	-5.21	930	0.047	0.04414063	-6.08
655	0.042	0.03970703	-5.46	935	0.046	0.04325781	-5.96
660	0.042	0.03970703	-5.46	940	0.047	0.04414063	-6.08
665	0.043	0.04059766	-5.59	945	0.046	0.04325781	-5.96
670	0.043	0.04059766	-5.59	950	0.047	0.04414063	-6.08
675	0.042	0.03970703	-5.46	955	0.046	0.04325781	-5.96
680	0.042	0.03970703	-5.46	960	0.046	0.04325781	-5.96
685	0.043	0.04059766	-5.59	965	0.046	0.04325781	-5.96
690	0.042	0.03970703	-5.46	970	0.045	0.04237500	-5.83
695	0.043	0.04059766	-5.59	975	0.044	0.04148438	-5.72
700	0.044	0.04148438	-5.72	980	0.046	0.04325000	-5.98
705	0.043	0.04059766	-5.59	985	0.046	0.04325000	-5.98
710	0.043	0.04059766	-5.59	990	0.046	0.04325000	-5.98
715	0.044	0.04148438	-5.72	995	0.047	0.04414063	-6.08
720	0.043	0.04059766	-5.59	1000	0.045	0.04237500	-5.83
725	0.045	0.04237500	-5.83				

[27] F.-F. Wang, J.-J. Liu, C.-L. Li, X. Ren, L.-L. Mu, W. Yan, W.-R. Wang, J.-T. Xiao, X. Tan, X.-X. Zhang, X.-D. Zou, and X.-Y. Gao, "A new lunar absolute control point: Established by images from the landing camera on Change-3," Research in Astronomy and Astrophysics, vol. 14, no. 12, pp. 1543–1556, Dec. 2014.

[28] Y. Z. Wu, Z. C. Wang, W. Cai, and Y. Lu, "The Absolute Reflectance and New Calibration Site of the Moon," The Astronomical Journal, vol. 155, no. 5, p. 213, May 2018.